Silica-encapsulated intermetallic nanoparticles for highly active and selective heterogeneous catalysis

Minda Chen, <sup>1</sup> Russ Bowers, <sup>2,\*</sup> Wenyu Huang <sup>1,3,\*</sup>

<sup>1</sup>Department of Chemistry, Iowa State University, Ames, IA 50011, United States

<sup>2</sup>Department of Chemistry, University of Florida, Gainesville, FL 32611, United States

<sup>3</sup>Ames Laboratory, U.S. Department of Energy, Ames, IA 50011, United States

\*Corresponding authors

#### **Abstract conspectus:**

Intermetallic nanoparticles (iNPs) have been the subject of many recent reports for their demonstrated applications as highly active and selective heterogeneous catalysts. As a subclass of alloys, intermetallic compounds possess ordered crystal structures and, therefore, well-defined atomic environments, unlike the solid solution of alloys whose atomic arrangements are random and locally unpredictable. Catalytically-active iNPs typically contain a group 8-10 transition metal as the "active" metal. They also include an "inactive" metal that does not directly participate in the catalytic reaction but can significantly modify the active metal's behavior. The choice of the inactive metal component can range across the periodic table.

A few general challenges remain to design iNPs for heterogeneous catalysts with outstanding performance. Synthetically, the high surface energy of small nanoparticles is prone to their aggregation, while maximizing the surface-to-volume ratios is highly desired for efficient noble metal utilization. Additionally, even though the formation of bulk intermetallic compounds has been extensively studied, the formation of intermetallic phases at the nanoscale can behave differently. For example, the formation temperatures of iNPs are often drastically different from those predicted from the bulk phase diagrams. This behavior often leads to further challenges in the synthesis of iNPs.

In addition to synthetic challenges, it is also critical to demonstrate the performance of iNPs in catalysis and establish the structure-property relationships. Instrumental and computational techniques often assist the understanding of catalytic properties. Due to the long-range order of intermetallic structure, various electron and X-ray techniques have been used to precisely determine the structure of iNPs. Structural modeling in density functional theory (DFT) calculation can also benefit from such ordered structures. The establishment of structure-property relationships is critical for designing and synthesizing advanced catalysts targeting different catalytic reactions. iNPs have been employed for a great variety of reactions in thermo-, electro-, and photo-catalysis. Hydrogenation of furfural to furfuryl alcohol, for example, is a model reaction, where PtSn iNPs show enhanced activity and chemoselectivity in hydrogenating C=O rather than C=C bonds. This superior catalytic performance correlates to the change in the geometric and electronic surface structure of the PtSn iNPs. Additionally, intermetallic surfaces can be further modified by ligands or defects. While adding complexity to iNP systems, these modifiers provide additional control over their catalytic properties.

In this Account, taking encapsulated iNPs in mesoporous silica as an example, we review the current strategies to develop iNPs as highly performed heterogeneous catalysts, with insights on the distinct formation behavior of iNPs compared to bulk intermetallic materials. We then highlight thermo- and electro-catalysis reactions to which these iNP catalysts are applied. We also discuss the unique pairwise hydrogenation reaction with parahydrogen catalyzed by iNPs. In this reaction, iNPs show unparalleled potential. We anticipate that this Account could foster additional interests in studying intermetallic catalysts and lay the foundation for their applications.

#### 1. Introduction

It has been the goal of chemists to design catalysts with high activity, controllable selectivity, and long-term stability. The introduction of nanomaterials and the advancement of characterization techniques have revolutionized catalyst development in recent years. Numerous work has been devoted to the synthesis of nanocatalysts based on metal atoms or nanoparticles. The size control of the active metal in catalysts, ranging from individual atoms to hundreds of nanometers, represents one aspect of the latest technology in manipulating the synthesis of nanomaterials. Although many metal nanoparticles have been proven to be highly effective catalysts, chemists are still looking for strategies to improve their performance further. For example, involving strong metal-support interaction with different catalyst supports and alloying with other metals have been practiced to alter the electronic property or geometric environment of active metal sites.

One of such approaches is developing catalysts based on intermetallic compounds, alloys with ordered crystal structures. Many intermetallic systems containing precious metals have been studied for heterogeneous catalysis and exhibit outstanding catalytic properties compared to monometallic or random-alloy-type bimetallic catalysts.<sup>1-6</sup> Intermetallic catalysts have two major

advantages. First, they have well-defined atomic structures. Unlike random alloys whose atomic arrangements are largely unpredictable, intermetallics have precisely determined crystallographic structures, leading to uniform active sites. The well-defined structures enable iNPs to be easily studied by advanced characterization techniques, such as aberration-corrected scanning transmission electron microscopy (STEM) and X-ray absorption spectroscopy (XAS). Secondly, the formation of intermetallic structures is enthalpy-driven. As a result, iNPs have high stability against catalyst deactivation associated with phase segregation, carbide/hydride formation, and metal leaching.

While various intermetallic systems have been explored in heterogeneous catalysis, many challenges remain to be solved. The efficient utilization of precious metals, one of the most important factors of supported metal catalysts, can only be achieved with ultrasmall metal nanoparticles but is synthetically challenging.<sup>7,8</sup> The current synthesis of iNPs generally employs impregnation or precipitation methods, followed by high-temperature oxidation/reduction and annealing, during which particle aggregation easily leads to inefficient metal utilization. In addition, while solid-state chemists studied the synthesis of bulk intermetallic materials extensively, iNPs could require distinctly different synthetic conditions due to the significance of surface for nanomaterials. Besides the synthetical challenge, it is also critical to further understand the catalytic behavior at the atomic level.<sup>9</sup> In an intermetallic catalyst, the addition of a secondary "inert" metal that is not catalytically active provides different types of modification to the behavior of the active metal. One previous review summarizes them as electronic, geometric, steric, and ordering effects.<sup>3</sup> Improving our understanding of intermetallic effects in catalysis is not trivial and requires a combination of characterization and computation techniques.<sup>10,11</sup>

## 2. Structural design of silica-encapsulated iNPs

## 2.1. Development of synthetic routes

Inspired by the use of organic capping agents to prevent particle aggregation and achieve high particle monodispersity, we introduced a "ship-in-a-bottle" strategy using inorganic mesoporous SiO<sub>2</sub> shell (mSiO<sub>2</sub>) to encapsulate bimetallic/intermetallic nanoparticles and achieve the same purposes.<sup>12,13</sup> Core-shell type structures made by encapsulating metal nanoparticles in mesoporous oxide material have several beneficiary features for their applications, such as high surface area, monodisperse particle size, tunable pore diameter/length, controlled pore morphologies, and self-assembly capabilities.<sup>14</sup> The mSiO<sub>2</sub>-encapsulated metal nanoparticles (M@mSiO<sub>2</sub>) are stable against thermal treatment above 500 °C, and thus a suitable platform to synthesize iNPs that typically require high-temperature annealing. In general, monometallic M<sub>1</sub> nanoparticles are first encapsulated by mSiO<sub>2</sub> shell, and the precursor of a second metal M<sub>2</sub> is subsequently reduced at the surface of M<sub>1</sub>. The mSiO<sub>2</sub> shell that closely interacts with M<sub>1</sub> nanoparticles is partially etched during the process, providing space for the growth of bimetallic nanoparticles.<sup>13</sup> With proper thermal and chemical treatment, various nanostructures can be made (Figure 1a).

In particular, this approach enables us to synthesize iNPs with high monodispersity and improved thermal stability. High-temperature treatments are usually required to form intermetallic structures due to the energy barriers to rearrange metal atoms. The mSiO<sub>2</sub> shell, therefore, provides physical protection for the nanoparticles against sintering and aggregation during thermal treatments. Various Pt-based iNPs have been synthesized by this approach, such as Pt<sub>3</sub>Sn, PtSn, PtZn, and PtPb. TEM images of Pt@mSiO<sub>2</sub> (size of 14.3 ± 0.8 nm) and PtSn@mSiO<sub>2</sub> (size of 20.6 ± 0.9 nm) are shown in Figure 1b. With aberration-corrected STEM, the ordered atomic structure of PtSn is confirmed, matching PtSn intermetallic phase. <sup>15</sup> Energy-dispersive X-ray spectroscopy

(EDS) mapping confirms the even distribution of Pt and Sn within the nanoparticle (Figure 1c).  $^{16}$  Using smaller Pt nanoparticles as cores, we also demonstrate the synthesis of  $\sim$ 7 nm PtSn@mSiO<sub>2</sub>,  $^{17}$  with a high surface to volume ratio for efficient utilization of precious metal in heterogeneous catalysis.

To further enhance the surface utilization of iNPs and benefit their application in electrocatalysis, ultrasmall PtZn nanoparticles ( $3.2 \pm 0.4$  nm) are made through a similar approach (Figure 1d-e). Multi-walled carbon nanotubes (MWNTs) are selected as support for the initial deposition of Pt precursors. After growing the mSiO<sub>2</sub> shell, a reduction treatment leads to the formation of ultrasmall and highly monodisperse Pt nanoparticles ( $2.1 \pm 0.3$  nm) due to the confinement of mSiO<sub>2</sub> that restricts the possible aggregation and sintering of nanoparticles. Due to the protection of mSiO<sub>2</sub>, nanoparticles remain small and monodisperse after incorporation of Zn and annealing at 600 °C for the formation of PtZn intermetallic phase. The mSiO<sub>2</sub> shell is selectively removed by etching for electrocatalysis purposes. Catalytic performance of the PtZn iNPs is highly benefited from their small size and high monodispersity, as demonstrated in section 3.1. Similarly, using NH<sub>2</sub>-functionalized 200 nm SiO<sub>2</sub> spheres to replace the MWNTs, we synthesized  $3.9 \pm 0.3$  nm PtSn iNPs confined at the interface between the solid SiO<sub>2</sub> sphere core and the mSiO<sub>2</sub> porous shell, representing another approach to obtain small intermetallic catalysts. In

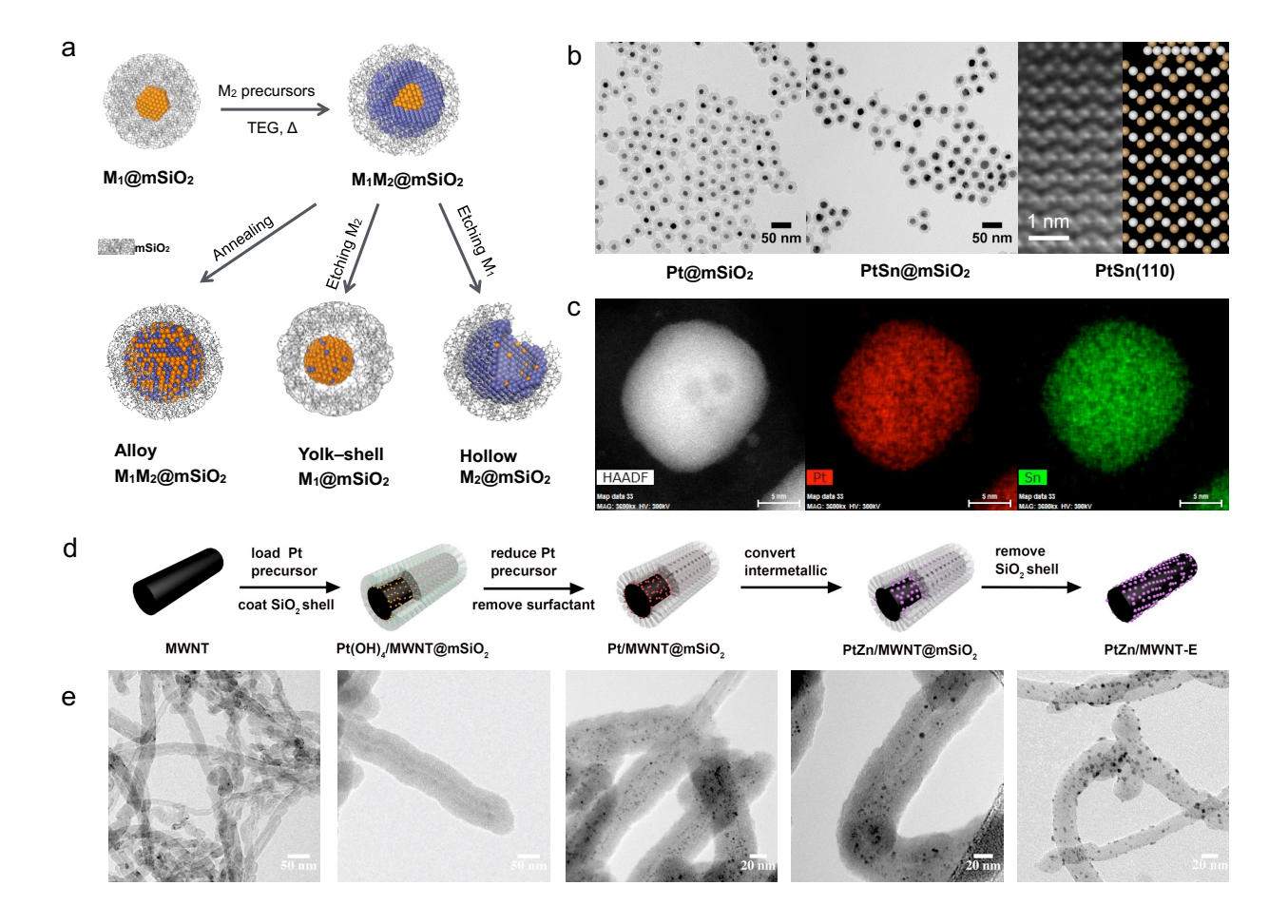


Figure 1. (a) Schematic illustration of a seeded growth approach with inorganic SiO<sub>2</sub> capping agent to synthesize bimetallic M<sub>1</sub>M<sub>2</sub>@mSiO<sub>2</sub>, and its derived structures. (b) TEM images of Pt@mSiO<sub>2</sub>, PtSn@mSiO<sub>2</sub>, and an HR-TEM image of the PtSn atomic structure. (c) EDS elemental mapping of Pt and Sn in the PtSn@mSiO<sub>2</sub> structure. (d) Schematic illustration and (e) corresponding TEM images of a seeded growth approach using SiO<sub>2</sub> capping to synthesize ultrasmall PtZn nanoparticles on MWNTs. (a) reproduced with permission from ref <sup>13</sup>. Copyright 2015 Royal Society of Chemistry. (b) reproduced partially from ref <sup>15</sup>. Copyright 2020 Royal Society of Chemistry. (c) reproduced with permission from ref <sup>16</sup>. Copyright 2017 Elsevier. (d) and (e) reproduced with permission from ref <sup>18</sup>. Copyright 2017 American Chemical Society.

### 2.2. Unique formation behavior at nanoscale

Successful in making iNPs, we are curious about the divergence in the formation condition of intermetallic phases at nanoscale from bulk intermetallic compounds. The formation of bulk intermetallic materials has been studied extensively in solid-state chemistry, summarized by binary phase diagrams. While the Pt-Sn phase diagram documents a eutectic point of >1200 °C for the PtSn phase, we have experimentally determined that <300 °C is sufficient in making pure phase PtSn iNPs of 7 and 20 nm in diameter. This type of discrepancy is commonly observed in synthesizing iNPs, emblematic of a general difference in the formation behavior of bulk and nanosized intermetallic materials. To better understand the difference, we studied the formation of iNPs with powder X-ray diffraction (PXRD) and *in-situ* STEM.

With two distinct sizes of Pt@mSiO<sub>2</sub> nanoparticles (5 and 14 nm in Pt diameter), it became possible to reveal the size-dependence of the Pt to PtSn transformation. Monitoring such phase transformation was achieved through *ex-situ* sampling and PXRD during the process. The PXRD results, containing mixed diffraction patterns of Pt and PtSn phases, were deconvoluted and quantified to calculate α, the conversion of Pt. Figure 2a,b show the results for 5 and 14 nm Pt@mSiO<sub>2</sub> nanoparticles, respectively, at three temperatures. A divergence of the two sizes is shown in the rapid initial conversion and apparent slow-down of transformation at a later stage for the 14 nm Pt@mSiO<sub>2</sub>. However, such a two-stage transformation is not observed for the 5 nm Pt@mSiO<sub>2</sub>. We believe that the nanoparticle surface is majorly responsible for the discrepancy, and ultimately, between nano-sized and bulk intermetallic materials.

A proposed mechanism (Figure 2c) is established for the Pt to PtSn phase transformation. For the 14 nm Pt@mSiO<sub>2</sub> nanoparticles, the amount of Pt atoms at/near the surface is not dominant. Therefore, as the Sn precursor is reduced on the surface of Pt, Sn atoms rapidly intermix with Pt

to form PtSn intermetallic phase at the surface, accounting for the initial fast conversion of Pt. In later research on the formation of intermetallic phase using *in-situ* STEM,<sup>20</sup> we also discovered the existence of intermediate Pt<sub>3</sub>Sn phase, and that the Pt<sub>3</sub>Sn/PtSn interface lowers the activation energy of phase transformation. As the surface is fully covered by PtSn intermetallic, the continuing of intermetallic formation depends on the diffusion of Pt and/or Sn atoms through the solid intermetallic layer, which is significantly slower and is described previously by solid-state diffusion models. These two stages combine to represent the phase transformation behavior of the 14 nm Pt@mSiO<sub>2</sub>. For the 5 nm Pt@mSiO<sub>2</sub> nanoparticles, however, the high surface-to-volume ratio minimizes the contribution from the second diffusion stage, and thus only the first surface intermixing stage is observed by PXRD. Therefore, the surface contribution for the formation of bulk intermetallic compounds could be entirely masked by the dominant inner atoms that require a much higher temperature to facilitate the slow atomic diffusion kinetics.

In addition, we recently investigated the formation of the PdSn iNPs (Figure 2d).<sup>21</sup> Although PdSn is a eutectic intermetallic phase on the Pd-Sn binary phase diagram, previous studies mostly focused on the thermodynamically preferred Pd<sub>3</sub>Sn<sub>2</sub> phase. With *in-situ* PXRD and XAS characterization, we discovered that the PdSn phase is metastable. While forming at >550 °C annealing, it readily reverts to the stable Pd<sub>3</sub>Sn<sub>2</sub> phase during slow or normal cooling processes. Using a quenching method to achieve fast cooling, we preserved the PdSn phase at room temperature. Our model hydrogenation reaction and carbon monoxide diffuse reflectance Fourier transform infrared spectroscopy (CO-DRIFTS) results suggest that the rapid cooling process successfully prevents the atomic structure change at the nanoparticle surface, the key to designing catalysts with enhanced performance.

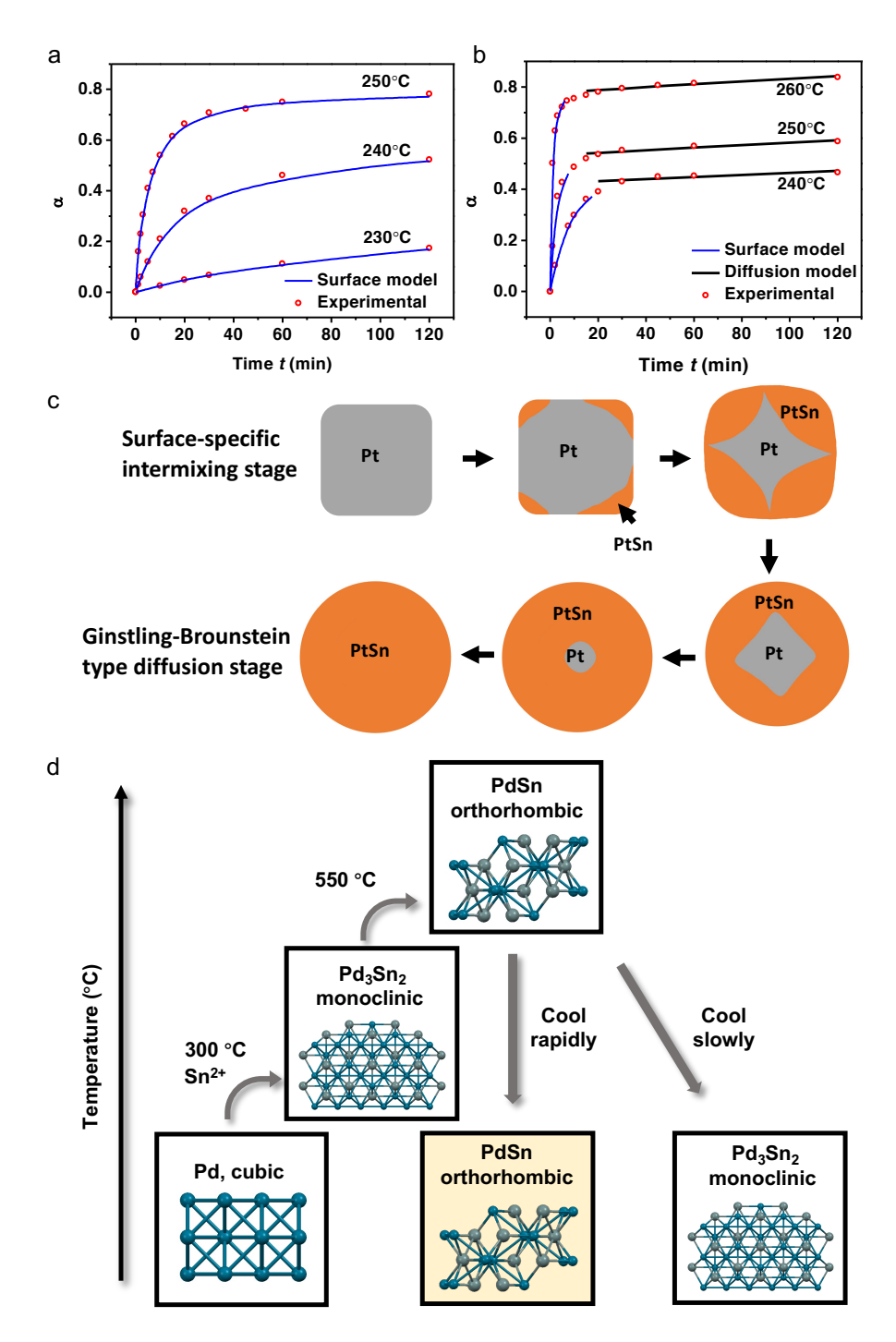


Figure 2. The transformation kinetics from Pt to PtSn monitored by time-evolution PXRD studies with (a) 5 and (b) 14 nm Pt nanoparticles. (c) Schematic illustration of a proposed mechanism for the Pt to PtSn phase transformation, showing the surface intermixing stage that is dominant on smaller nanoparticles and the bulk-like diffusion stage that is majorly responsible for

transformation of larger nanoparticles. (d) Schematic illustration of a quenching method used to form pure phase PdSn nanoparticles, and a natural cooling process lead to mixed phase. (a)-(c) Reproduced with permission from ref <sup>17</sup>. Copyright 2020 Royal Society of Chemistry. (d) Reproduced with permission from ref <sup>21</sup>. Copyright 2021 Wiley.

### 3. Active site engineering on intermetallic structure to achieve high catalytic performance

## 3.1. Surface geometric and electronic effect on iNPs

The catalytic properties of heterogeneous catalysts are primarily governed by their surface. For the preparation of bimetallic and intermetallic nanocatalysts, an ideal synthetic methodology should be able to generate a variety of catalysts whose structure can be tailored towards different reactions with excellent performance.<sup>22</sup> To achieve such desired catalytic performance, it is ultimately necessary to engineer the surface atomic structure and composition to achieve optimum geometric and electronic properties.<sup>23-25</sup>

As discussed earlier, Pt-M@mSiO<sub>2</sub> (where M = Sn, Zn, Pb) demonstrated the generation of thermally stable iNPs confined within a mesoporous silica environment. To evaluate the catalytic properties, we compared the performance of intermetallic PtSn@mSiO<sub>2</sub> to the monometallic Pt@mSiO<sub>2</sub> for the selective hydrogenation of furfural to furfuryl alcohol (Figure 3a). With the same quantity of noble metal content, PtSn@mSiO<sub>2</sub> showed complete conversion of furfural to furfuryl alcohol at >97% selectivity, while Pt only gave lower conversion (24%) and furfuryl alcohol selectivity (35%) with many hydrogenolysis side products. When we compared the activity normalized to surface Pt sites measured by chemisorption, the activity of PtSn is ~40 times greater than Pt in selective hydrogenate C=O in furfural. These results suggest that PtSn@mSiO<sub>2</sub> has a

superior activity and selectivity in hydrogenating C=O bonds over C=C bonds and preventing other side reactions, e.g., hydrogenolysis of C-C or C-O bonds.

The rationale behind this superior performance of PtSn intermetallic surface in furfural hydrogenation was made clear by DFT studies (Figure 3b). Compared to Pt(111), the PtSn(110) surface, one of the most stable surfaces identified by DFT, has a more open surface structure with parallel chains of Pt atoms interspersed with Sn atoms. These surface structural differences affect the adsorption configuration of furfural. On the Pt(111) surface, furfural preferably adsorbs in a flat orientation, with the C=C bonds in the furan ring and the C=O bond positioned across Pt-Pt bridge sites. The adsorbed hydrogen atoms at adjacent Pt atoms subsequently react with the adsorbed furfural at multiple bonds, leading to a range of products and a low selectivity. On PtSn(110) surface, lacking the closely packed Pt atoms, furfural favors the adsorption by the C=O moiety on the surface, while the rest of the molecule dangles above the catalyst surface in a standing configuration. Hydrogen atoms adsorbed at the bridge sites of the more open-structure Pt chains then hydrogenate the C=O bond alone, leading to the higher selectivity to furfuryl alcohol.

The introduction of Sn also changes the electronic structure of Pt and thus the binding strength of furfural at the surface of the nanoparticle. Binding strength of a substrate to a surface is related to the *d*-band position of the metal from the Fermi Level.<sup>23</sup> The more low-lying the *d*-band of the catalytically active metal, the weaker the binding strength of the adsorbate. In the case of PtSn@mSiO<sub>2</sub>, the donation of electrons from Sn to Pt pushes the *d*-band center of Pt further away from the Fermi level, leading to weaker adsorption of furfural at the PtSn(110) surface. In contrast, at the Pt(111) surface, furfural adsorbs strongly via multiple C-Pt bonds, leading to a mixture of products during hydrogenation, which is likely the reason for its lower activity.

Following up on the study of furfural hydrogenation, we showcased another structure-property relationship study of intermetallic PtSn surface using selective nitrostyrene hydrogenation. With both nitro- and vinyl- groups present in nitrostyrene, it is generally preferred to solely hydrogenate the nitro to amino group. We chose Pt monometallic nanoparticles, Pt<sub>3</sub>Sn, and PtSn iNPs as three benchmark catalysts to evaluate their catalytic performance in nitrostyrene hydrogenation. PtSn iNPs show >99% selectivity to convert 3-nitrostyrene to 3-aminostyrene, though with a low reaction rate (Figure 3c). In sharp contrast, Pt<sub>3</sub>Sn and Pt facilitate rapid hydrogenation of both nitro and vinyl groups with no preferential selectivity.

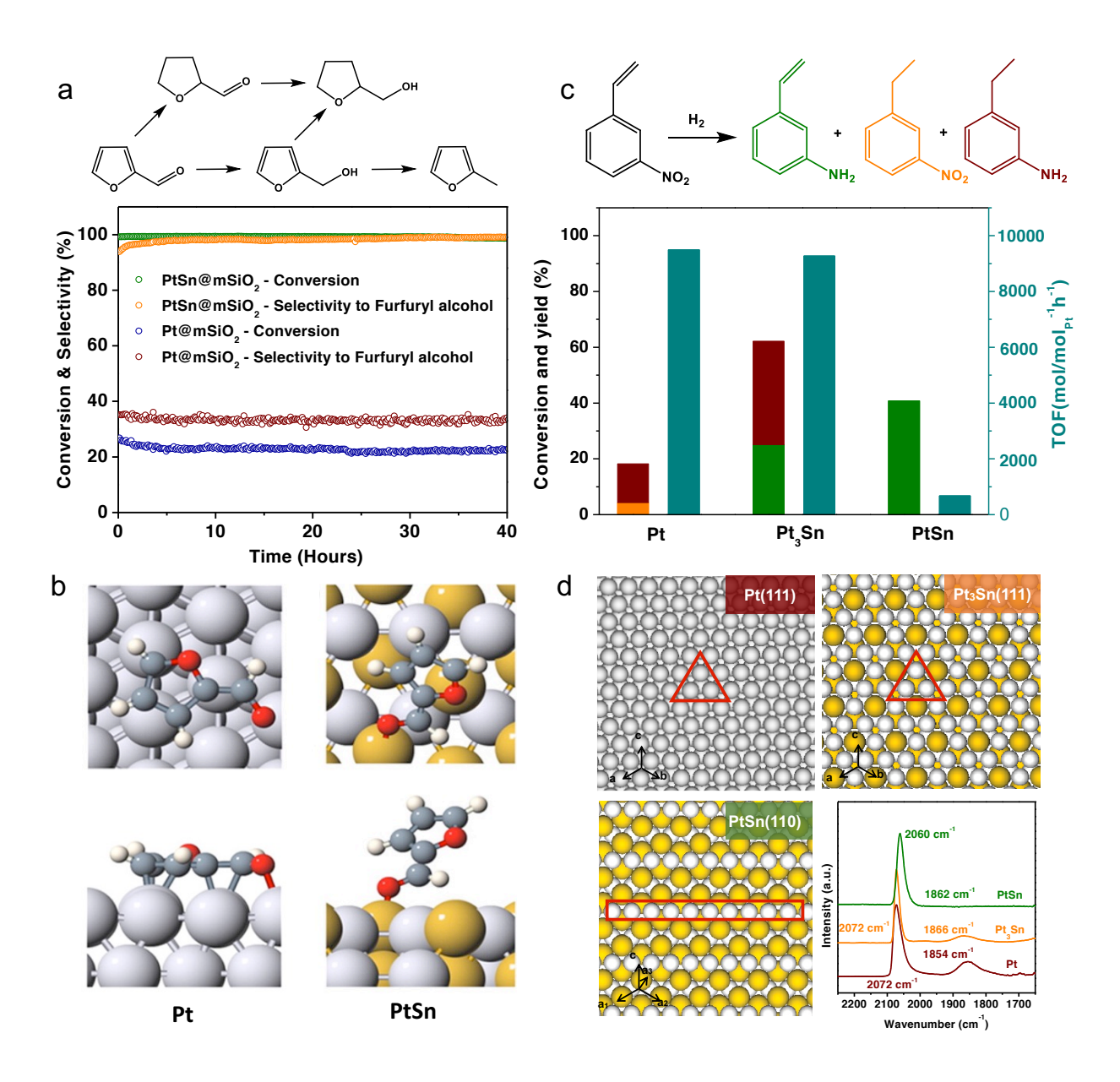


Figure 3. Control of catalytic properties by surface geometric effect over iNPs. (a) Comparing the performance of Pt@mSiO<sub>2</sub> and PtSn@mSiO<sub>2</sub> catalysts on selective hydrogenation of furfural. Reaction condition: furfural/H<sub>2</sub>/He = 0.023/11.4/8.6 mL/min, 6.4 μmol Pt in each catalyst, 160 °C. (b) The DFT-calculated most preferred configuration of furfural on Pt(111) and PtSn(110) surfaces. (c) Comparing the performance of Pt@mSiO<sub>2</sub>, Pt<sub>3</sub>Sn@mSiO<sub>2</sub>, and PtSn@mSiO<sub>2</sub> on selective hydrogenation of 3-nitrostyrene. The yields to different products are color-coded in the reaction scheme. Reaction condition: 1 mg catalyst, 50 mg 3-nitrostyrene, 20 mg xylene as internal

standard, 2 mL toluene, 80 °C, and 20 bar H<sub>2</sub>. Reaction time was tuned for Pt (0.16 h), Pt<sub>3</sub>Sn (0.16 h), and PtSn (6 h) to adjust conversion levels to 18.2, 62.2, and 40.8%, respectively. Turnover frequency (TOF) of each catalyst was calculated at *ca*. 10-20% conversion. (d) Atomic geometry of Pt(111), Pt<sub>3</sub>Sn(111), and PtSn(110) surfaces showing the Pt<sub>3</sub> trifold sites (red triangle) and Pt<sub>2</sub> bridged sites (red rectangle), and the corresponding DRIFTS results indicating the CO adsorption modes on these surfaces. (a) and (b) reproduced with permission from ref <sup>12</sup>. Copyright 2016 American Chemical Society. (c) and (d) reproduced with permission from ref <sup>16</sup>. Copyright 2017 Elsevier.

The high selectivity to the hydrogenation of nitro group on the PtSn surface reflects the intrinsic structural advantages of the PtSn intermetallic surface as it lacks threefold Pt<sub>3</sub> sites. CO-DRIFTS results (Figure 3d) prove the absence of Pt<sub>3</sub>-adsorbed CO on PtSn surface. Since Pt<sub>3</sub> sites are proposed to be the active site for H<sub>2</sub> dissociation,<sup>26</sup> we proposed a non-Horiuti-Polanyi hydrogenation pathway (non-dissociation of H<sub>2</sub>) proceeding over PtSn iNPs. Due to the lack of atomic hydrogen, PtSn has a much lower activity in both apparent reaction rate and turnover frequency (TOF). Unlike PtSn, Pt<sub>3</sub>Sn and Pt are more prone to surface saturation with atomic H, and present similar TOFs much higher than that of PtSn iNPs. This study brings molecular-level understandings of surface structures of PtSn in dramatically alternating their hydrogenation performance, which brings the possibility of engineering catalyst structures for different reactions.

As previously described, the mesoporous silica encapsulation strategy enables the synthesis of sub-4 nm PtZn iNPs on conductive MWNTs support. After removing the protective mSiO<sub>2</sub> shell, the PtZn/MWNTs show good conductivity for electrocatalysis. Applied to the electrocatalytic methanol oxidation (MOR) reaction, these small PtZn iNPs exhibited about 10 times higher mass

activity in both acidic and basic solutions compared to larger PtZn iNPs prepared without the confinement provided by the porous silica shell (Figure 4a-b). More interestingly, the specific activity is also enhanced with the smaller particle size, indicating the active sites on smaller PtZn iNPs are more active than those on larger ones.

DFT calculation (Figure 4c) was employed to study MOR pathways over PtZn(111), stepped PtZn(211), and Pt<sub>24</sub>Zn<sub>24</sub> cluster, which represent terrace, edge, and corner sites, respectively. All three PtZn systems undergo a "non-CO reaction pathway", where a key intermediate CH<sub>2</sub>O\* is formed and further reacted with OH\* to yield H<sub>2</sub>COOH\*. After a (H\* + e\*) pair is released, the formed HCOOH\* then goes through either COOH\* or HCOO\* to form the final product CO<sub>2</sub>. The calculation suggests that the reaction pathway on Pt<sub>24</sub>Zn<sub>24</sub> has the smallest apparent barriers, potentially due to the enhanced binding strength between the intermediates and the undercoordinated metal atoms on the corner sites. These results indicate that the smaller PtZn iNPs are energetically more favorable for MOR. In contrast, MOR on Pt(111) surface undergoes a "CO reaction pathway", forming the COH\* and CO\* intermediates. The CO\* is then converted to COOH\*, and finally CO<sub>2</sub>. As the formed COH\* and CO\* are highly stable on Pt surface, the further reaction to CO<sub>2</sub> is hindered, leading to CO poisoning of Pt catalyst. Besides, it is believed the stabilization of another key adsorbate, OH\*, by Zn atoms leads to the non-CO pathway over the PtZn system.

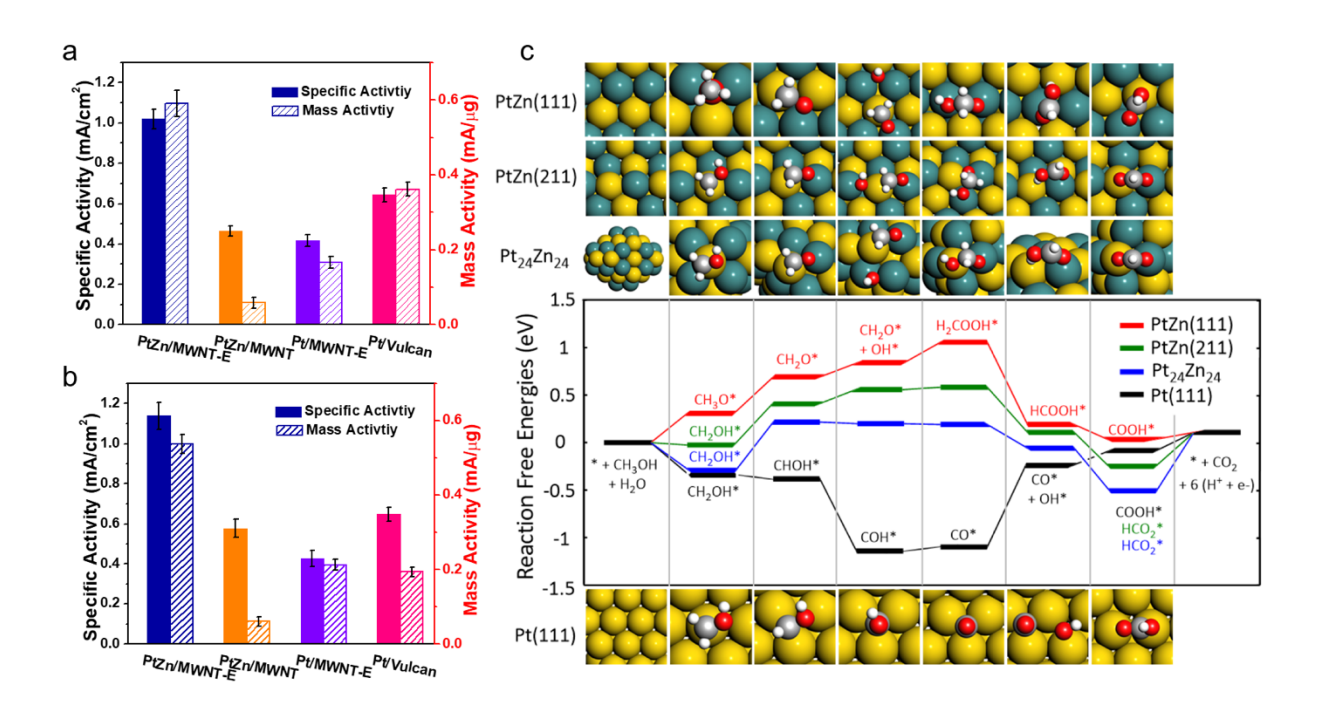


Figure 4. The enhanced performance of PtZn iNPs in catalytic electrooxidation reaction. The mass activity and specific activity of PtZn and Pt catalysts were compared under (a) acidic and (b) basic conditions toward the methanol oxidation reaction. (c) Calculated reaction free energies and pathways on various Pt and PtZn surfaces. Reproduced with permission from ref <sup>18</sup>. Copyright 2017 American Chemical Society.

## 3.2. Surface modifying ligands

Organic stabilizers have featured prominently in the synthesis of colloidal nanoparticles. Besides bestowing protection against agglomeration, they can also assist in the size and shape control of the synthesized nanoparticles. The persistence of these ligands, though, is traditionally considered detrimental to catalytic activity as they block the catalytic active sites.<sup>27</sup> Methods have been developed to minimize the presence of these ligands at the surface post their synthesis, but these methods can be cumbersome and add to the complexity of catalyst preparation.<sup>28,29</sup>

Interestingly, recent studies in the synthesis of bimetallic and intermetallic nanoparticles employ ligands to improve catalytic performance. Fu et al. synthesized Pt<sub>3</sub>Co nanoparticles stabilized by oleylamine and demonstrated its role in the hydrogenation of cinnamaldehyde.<sup>30</sup> The long-chain ligand sterically restricts the adsorption of the incoming substrate by only allowing the terminal C=O group to access the metal nanoparticle surface for subsequent hydrogenation, therefore, resulting in high chemo-selectivity and low activity. For further improvement on this catalytic reaction, Rodionov et al. prepared Pt-Fe bimetallic nanoparticles using oleic acid instead of oleylamine, applying the same steric hindrance model to restrict adsorption modes of substrates at the catalyst surface.<sup>31</sup> The use of oleic acid ligands improves the catalytic activity since ligands bind specifically to Fe sites, and thus access to Pt by cinnamaldehyde is less hindered. Furthermore, a perfluorinated analog of oleic acid enables higher activity with similar selectivity to the desired unsaturated alcohol.

These traditional colloidal synthesis methods cannot prepare iNPs free of capping ligand, which can be circumvented by our mesoporous silica encapsulation strategy. Using capping free Pt-Fe@mSiO<sub>2</sub> iNPs, we could decouple the effect of capping ligands from the inherent electronic and geometric structure of intermetallic surfaces on their activity and selectivity in cinnamaldehyde hydrogenation. Owing to the enhanced thermal stability, Pt-Fe@mSiO<sub>2</sub> could be calcined and reduced at temperatures as high as 700 °C to obtain different intermetallic phases based on the incorporated Pt to Fe ratio. The catalytically active catalysts had lower quantities of Fe and corresponded to fcc Pt<sub>3</sub>Fe phase when characterized by PXRD. While the catalysts prepared by Rodionov et al., with ligands other than the perfluorinated analogs, demonstrated poor selectivity to the unsaturated alcohol,<sup>31</sup> the Pt-Fe@mSiO<sub>2</sub> catalysts showed substantially higher selectivity to cinnamyl alcohol in the absence of surface modifying ligands.

Another benefit of the inorganic mSiO<sub>2</sub> encapsulation strategy is that we can easily probe capping effect on iNPs by adding different organic ligands post-synthetically. We conducted experiments by adding perfluorinated oleic acid to the reduced catalyst by impregnation. Conversion of cinnamaldehyde is doubled compared to pristine Pt-Fe@mSiO<sub>2</sub>, while maintaining high selectivity. Hence, the perfluorinated ligand can also be added post-synthesis of the nanoparticles for improved results. This study provides a new strategy with the flexibility to control catalytic selectivity.

#### 4.3. Intermetallic nanoparticles with non-stoichiometric composition

An ideal intermetallic structure has a fixed stoichiometry, and it is interesting how the crystal structure tolerates slight compositional deviations, especially at nanoscale. These deviations make the iNPs slightly off-stoichiometric but are not sufficient to make them favor other intermetallic phases.<sup>21,32,33</sup> In case this off-stoichiometric composition causes more structure changes on the surface than the bulk of iNPs, it could have a profound impact on their catalytic properties.

In principle, there are a few ways an iNP, consisting of metals M¹ and M² in specific ratio, could accommodate additional M² atoms beyond its fixed stoichiometry.³ First, those M² atoms could replace the position of M¹ atoms in the intermetallic structure, forming a (M¹<sub>x</sub>M²<sub>1-x</sub>)M²<sub>y</sub> structure and leading to size change of the crystallographic unit cell that is usually detectable with PXRD.³<sup>4</sup> Secondly, the M² atoms could dissolve in the intermetallic structure without an intrinsic order, similar to solid solution alloys. Lastly, M² atoms could reside in a segregated region, such as the core or the surface of the nanoparticles.

To understand these possibilities and their impacts on the catalytic properties of iNPs, we investigated the PtSn@mSiO<sub>2</sub> iNPs by intentionally deviating the Pt/Sn stoichiometric ratio from 1.0 to 1.2 and 0.9 (Figure 5). Pt<sub>1.2</sub>Sn@mSiO<sub>2</sub> at a Pt-rich stoichiometry shows a mixed crystalline

phase of Pt and PtSn with PXRD and XAS. EDS mapping locates the Pt at the core of the nanoparticles, forming a Pt@PtSn core-shell structure. Meanwhile, the Sn-rich Pt<sub>0.9</sub>Sn@mSiO<sub>2</sub> also exhibits a slightly Pt-rich core after 300 °C reduction and becomes homogeneous after 500 °C reduction.

More importantly, the surface of the nanoparticles was studied using furfural hydrogenation and acetylene semi-hydrogenation as probe reactions, along with CO-DRIFTS, to correlate the surface structural change with the catalytic behavior. We calculated the apparent activation energy for furfural hydrogenation on the Pt<sub>1.2</sub>Sn surface (16-18 kJ/mol) to be very close to that on the Pt surface (Figure 5a), indicating the existence of Pt contiguous sites at the nanoparticle surface. Interestingly, while the Sn-rich Pt<sub>0.9</sub>Sn surface also shows an activation barrier similar to Pt after 300 °C reduction, the activation barrier increases with a 500 °C reduction treatment and aligns closely with the stoichiometric Pt<sub>1.0</sub>Sn surface. This trend is supported by the shift of atop CO adsorption peak in CO-DRIFTS (Figure 5b). The Pt<sub>1.0</sub>Sn surface has an atop CO peak at 2068 cm<sup>-1</sup> <sup>1</sup>, lower wavenumber compared to that of Pt (2073 cm<sup>-1</sup>) due to the electron donation from Sn to Pt. The Pt<sub>1.2</sub>Sn surfaces, regardless of the reduction temperature, have an atop CO peak at a similar position with Pt, confirming the surface Pt contiguous sites. While Pt<sub>0.9</sub>Sn also shows the Pt-like peak after a 300 °C reduction, it shifts towards a PtSn-like peak after a 500 °C reduction. Therefore, we believe that the Pt-rich Pt<sub>1.2</sub>Sn possesses a Pt core and a Pt-rich surface where Pt sites are ensembled after reduction at either 300 or 500 °C (Figure 5c). The Sn-rich Pt<sub>0.9</sub>Sn possesses a similar Pt-rich surface at a lower reduction temperature (300 °C). However, structural reconstruction happens at a higher reduction temperature (500 °C) that homogenizes the nanoparticle to a well-ordered PtSn surface.

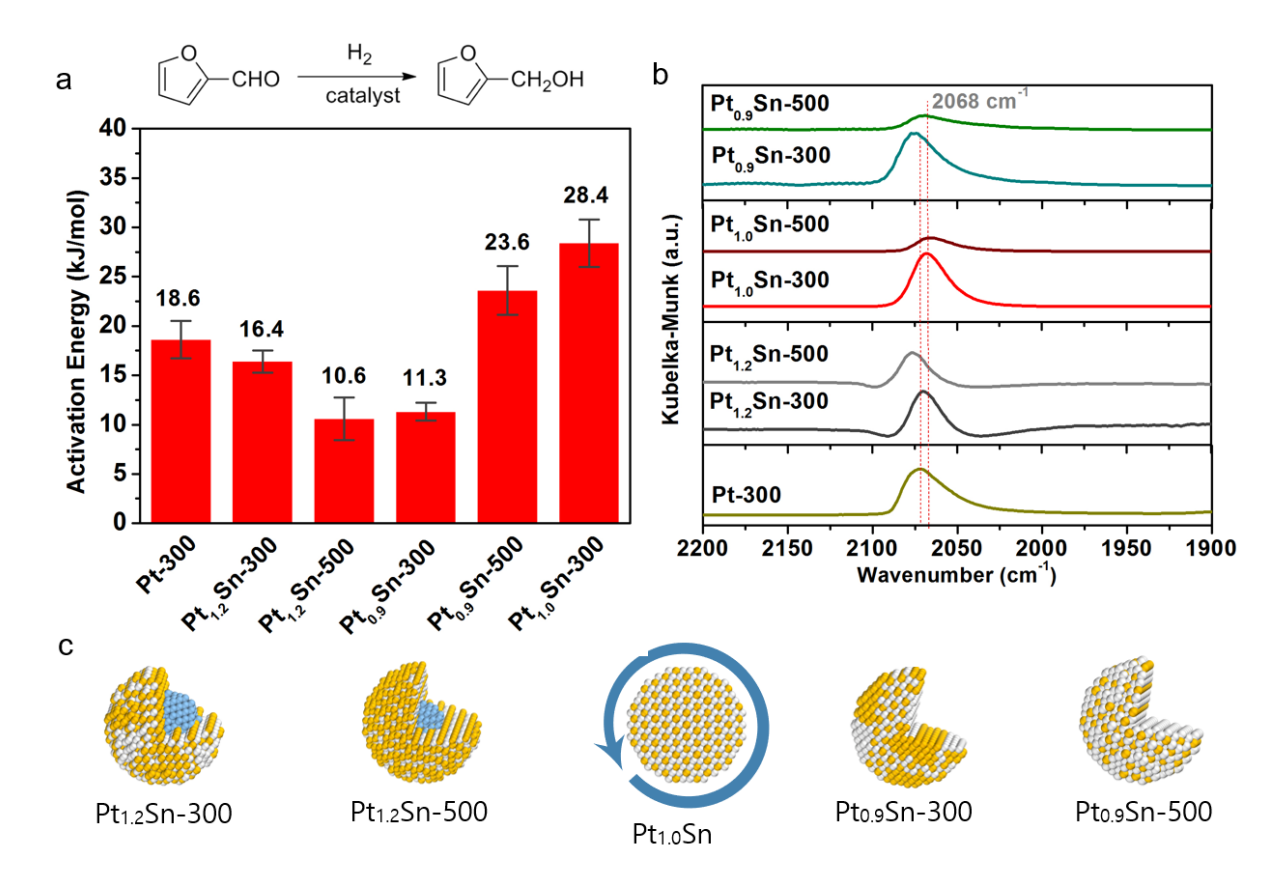


Figure 5. The study of non-stoichiometric PtSn surfaces. (a) The apparent activation barrier of furfural hydrogenation over Pt and various PtSn surfaces. (b) CO-DRIFTS spectra demonstrating the different CO peak positions adsorbed on Pt and various PtSn. (c) Proposed structural model for the Pt-rich, stoichiometric, and Sn-rich PtSn nanoparticles. Reproduced with permission from ref <sup>35</sup>. Copyright 2019 Elsevier.

### 4. iNPs for effective pairwise hydrogenation

Pairwise addition is a unique subclass of hydrogenations in which both protons from the same H<sub>2</sub> molecule are transferred to one and the same unsaturated substrate molecule. Pairwise selectivity of hydrogenation refers to the fraction of adducts formed by pairwise addition, the remaining fraction being formed by random addition. While the pairwise selectivity may have no

signficance when the intent is to maximize reaction yield, it is of central importance when the goal is to conserve the singlet spin order of parahydrogen, where the proton spin state is given by:

$$\psi_{\text{para}} = \frac{1}{\sqrt{2}} \left( |\alpha\beta\rangle - |\beta\alpha\rangle \right)$$

Hydrogenation experiments with parahydrogen are feasible because parahydrogen gas is metastable for extended periods of weeks to months at ambient temperature. While parahydrogen is itself invisible to nuclear magnetic resonance (NMR), a concerted, pairwise addition into coupled, magnetically inequivalent sites can produce a non-equilibrium nuclear spin *hyperpolarization* that is observable by NMR.<sup>36</sup> The intensity of NMR signals derived from parahydrogen can exhibit enhancements exceeding four orders of magnitude relative to the conventional NMR signals obtained from the thermal equilibrium spin polarization. For a two proton system, the theoretical signal enhancement at 9.4 T (400 MHz) and 300 K is  $31,376 \times \phi$ ,<sup>37</sup> where  $\phi$  is the pairwise selectivity, ranging from  $\phi$ =0 for random addition, to  $\phi$ =1 for pairwise addition. The pairwise selectivity may be estimated from the ratio of the observed and theoretical signal enhancements.<sup>38</sup>

Supported metal nanoparticles would be ideally suited for the continuous production of hyperpolarized liquids from parahydrogen for use in in-vivo magnetic resonance imaging and spectroscopy. In contrast to homogeneous catalysis with dissolved metal complexes, heterogeneous catalysis is compatible with rapid and spontaneous separation of the hyperpolarized fluid from the catalyst material. However, owing to the Horiuti-Polanyi mechanism and the fast H ad-atom diffusion, noble metal surfaces provide a platform for efficient mixing and recombination of H atoms originating from different H<sub>2</sub> molecules. The efficiency of this randomization process depends on many factors, including the type of metal and properties of the metal-oxide support, loading,<sup>39,40</sup> and particle size.<sup>41</sup> Monometallic Pt nanoparticles exhibit high turnover rates in

hydrogenation, but the pairwise selectivity is typically <<1% for particle sizes larger than a few nm. Notably, atomically dispersed Pt deposited at ultra-low loadings by atomic layer deposition on cerium oxide supports exhibited a pairwise selectivity of up to 6% for propene hydrogenation.<sup>40</sup> Yet even higher pairwise selectivity can be realized by utilizing iNPs composed of an active metal (e.g., Pt) and an inactive metal (e.g., Sn). To interpret the improved pairwise selectivity of hydrogenation over Pt<sub>3</sub>Sn and PtSn iNPs, we drew on the extensive literature on adsorption and diffusion of hydrogen on Pt(111) and Pt<sub>3</sub>Sn(111) surfaces using ultrahigh-vacuum surface-science techniques and DFT calculations.<sup>42</sup> This literature suggests that the impressive performance of these catalysts in parahydrogen enhanced NMR can be achieved by tuning the delicate balance between facile activation of H<sub>2</sub> versus suppression of H ad-atom diffusion.

### 4.1 Pairwise hydrogenation of alkenes and alkynes over Pt, Pt<sub>3</sub>Sn, and PtSn iNPs

Tin, when combined with Pt in an iNP, strongly affects the pairwise selectivity of hydrogenation as well as total conversion. <sup>26</sup> Figure 6 presents the 400 MHz <sup>1</sup>H NMR spectra of propane formed by hydrogenation of propene over 10 mg of Pt@mSiO<sub>2</sub>, Pt<sub>3</sub>Sn@mSiO<sub>2</sub>, or PtSn@mSiO<sub>2</sub> iNPs. The lower set of spectra were acquired immediately after hydrogenation with pH<sub>2</sub>. In these ALTADENA (Adiabatic Longitudinal Transport After Dissociation Engenders Net Alignment) mode experiments, <sup>43</sup> gaseous propane is formed by hydrogenation with pH<sub>2</sub> in the Earth's magnetic field, and the gas is then transported through 1/16" PEEK tubing to the detection coil of the NMR probe at 9.4 T. The parahydrogen-enhanced NMR peaks exhibit a net alignment pattern, where the methyl peak "a" and methylene peak "b" exhibit pure emission and absorption phases, respectively. The upper set of spectra in Figure 6 were acquired after interrupting the flow and waiting for the nuclear spin polarization to fully relax to its thermal equilibrium value at 9.4 T. The percent conversion, obtained from the integrals of the thermally polarized propane and

propene peaks, were found at 300 °C to be similar for Pt@mSiO<sub>2</sub> (19.5 %) and Pt<sub>3</sub>Sn@mSiO<sub>2</sub> (17 %), but much smaller for PtSn@mSiO<sub>2</sub> (0.3 %). The drastic reduction is attributed to the absence of three-fold Pt hollow sites on the PtSn catalyst.

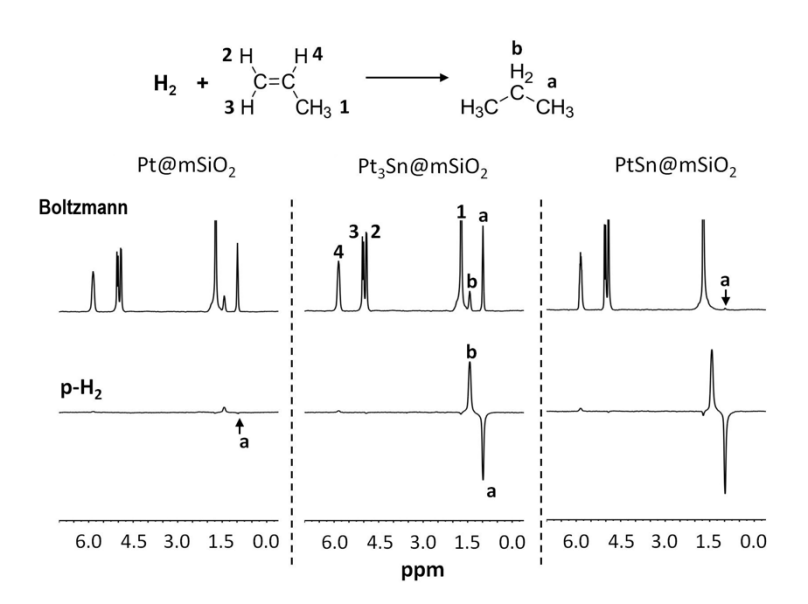


Figure 6. Parahydrogen enhanced NMR spectra acquired by hydrogenation of propene by Pt@mSiO<sub>2</sub>, Pt<sub>3</sub>Sn@mSiO<sub>2</sub>, and PtSn@mSiO<sub>2</sub> iNPs at 300 °C. The reactant gas mixture was 30% pH<sub>2</sub>, 52.5% propene, and 17.5 % N<sub>2</sub> at 400 mL/min total flow rate. All spectra are plotted on the same vertical scale. Reproduced with permission from ref <sup>26</sup>, copyright 2017 Wiley.

While conversion is strongly suppressed for PtSn@mSiO<sub>2</sub>, this catalyst nevertheless produced parahydrogen enhanced NMR signals with intensities similar to those for Pt<sub>3</sub>Sn, suggesting that the small conversion obtained under these reaction conditions is offset by an enormous increase in φ. Indeed, quantitative analysis indicates pairwise selectivities up to 11% for PtSn@mSiO<sub>2</sub>, which is more than three orders of magnitude more selective than hydrogenation over Pt@mSiO<sub>2</sub>. The dramatic increase in φ, accompanied by decreased conversion, is attributed to the absence of three-

fold Pt hollow sites (see Section 3) on the ordered PtSn(110). High vacuum studies of Pt(111) surfaces and Pt-Sn surface alloys have shown the three-fold Pt hollow sites to be essential for dissociative adsorption of H<sub>2</sub>.<sup>44</sup> Chemisorption of H<sub>2</sub> on the Pt<sub>2</sub>Sn(111) surface alloys at room temperature was found to be limited to only 2 % of the saturation coverage of hydrogen on clean Pt(111). In contrast, atomic hydrogen readily adsorbs on the alloy surfaces at temperatures down to 150 K, indicating that H<sub>2</sub> chemisorption is inhibited by kinetic rather than thermodynamic factors. The inability of the PtSn(110) surfaces to dissociate H<sub>2</sub> suggests that the elementary reaction step involves molecular H<sub>2</sub> as the reactant in either an Eley–Rideal or Langmuir–Hinshelwood type mechanism.

## 4.2 Hydrogenation of cyclopropane with parahydrogen over Pt-Sn iNPs

Hyperpolarized propane produced by heterogeneous hydrogenation of cyclopropane with parahydrogen has been proposed as a safe inhalant for sensitivity-enhanced in vivo magnetic resonance imaging.<sup>45</sup> Using 82% para-enriched H<sub>2</sub>, Chekmenev et al. showed that hydrogenation of cyclopropane over 118 mg of a Rh/TiO<sub>2</sub> catalyst yielded propane CH<sub>2</sub> signal enhancements (at 9.4 T) in the neighborhood of 480 (1.6% <sup>1</sup>H polarization) with <0.3% conversion, depending on catalyst loading, temperature, and flow rate. Parahydrogen enhanced NMR experiments were performed using Pt–Sn iNPs to explore the possibility of achieving higher polarization/conversion yield in the hydrogenation of cyclopropane.

Figure 7 shows the thermal equilibrium and ALTADENA spectra acquired for hydrogenation of cyclopropane at 300 °C using the mSiO<sub>2</sub>-encapsulated Pt and Pt-Sn iNP catalysts. The appearance of resonances "e" and "f" provides clear evidence for conversion to propane for all three catalysts. No products of hydrogenolysis such as methane or ethane were observed. Both Pt<sub>3</sub>Sn@mSiO<sub>2</sub> and PtSn@mSiO<sub>2</sub> yielded intense propane ALTADENA NMR signals. In addition to the propane

peaks, another set of resonances (a-d) also appear in the thermally polarized spectra of Figure 7a, revealing the presence of thermally polarized gaseous *propene* due to isomerization of cyclopropane. Notably, hyperpolarized propene was not observed, and isomerization to propene was not catalyzed by the Pt nanoparticles. The relative yields of propene and propane were observed to be temperature-dependent. Pairwise selectivity initially increased and then decreased with increasing temperature above 200 °C for Pt<sub>3</sub>Sn@mSiO<sub>2</sub>, while for PtSn@mSiO<sub>2</sub>, pairwise selectivity initially increased and then decreased above 350 °C. These results are consistent with an increasing number of thermally activated exchange steps with statistics favoring non-pairwise addition.

The accepted pathway for isomerization in the gas phase proceeds through the trimethylene biradical. He had analogy, the proposed mechanism for isomerization of cyclopropane on  $Pt_3Sn$  and  $PtSn@mSiO_2$  iNPs is shown as path "ii" in Figure 7b. After formation of  $\pi$ -bonded propene, either hydrogenation or desorption of propene can follow. In the presence of hydrogen, the propene can be subsequently hydrogenated with a high pairwise selectivity. To the extent that path "i" in Figure 7b also contributes to the products, the overall pairwise selectivity of hydrogenation of cyclopropane to propane will be diminished, which would lower the pairwise selectivity of hydrogenation of cyclopropane. The isomerization, not observed over the monometallic or Pt catalysts, is promoted by weakening of the propene–surface binding energy and depletion of the Pt adatom density.

To summarize, pairwise selectivity and conversion using the Pt<sub>3</sub>Sn catalyst were found to be comparable to that of the Rh/TiO<sub>2</sub> catalyst in Ref. <sup>12</sup>, while PtSn iNPs yielded a lower conversion. Unfortunately, significant amounts of propene were also produced using the Pt–Sn catalysts.

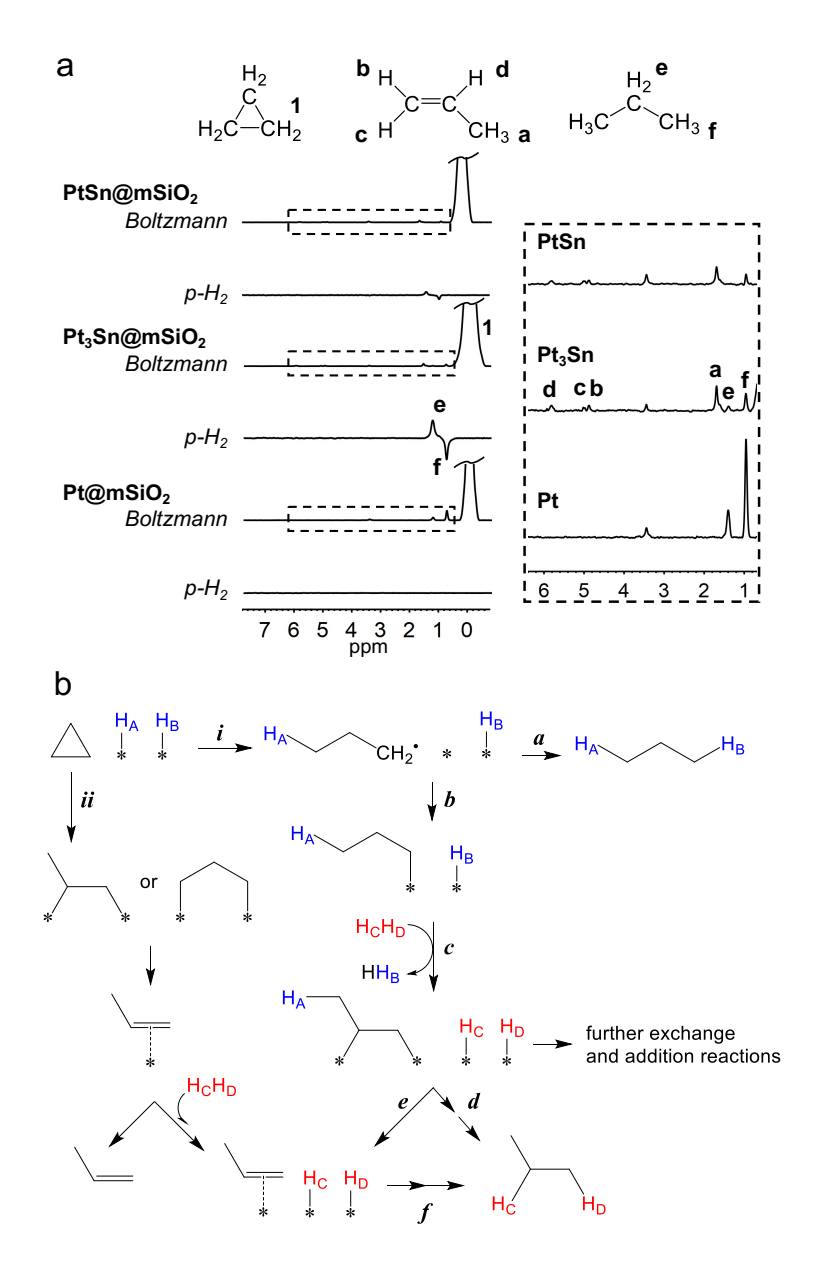


Figure 7. (a) Thermally polarized (top) and ALTADENA difference (bottom) spectra acquired using 120/70/210 mL/min of H<sub>2</sub>/N<sub>2</sub>/cyclopropane at 300 °C for PtSn@mSiO<sub>2</sub>, Pt<sub>3</sub>Sn@mSiO<sub>2</sub>, and Pt@mSiO<sub>2</sub>. ALTADENA and thermally polarized spectra were acquired with 32 and 512 transients, respectively. ALTADENA difference spectra were vertically scaled-up by a factor of 16 to facilitate direct comparison with the thermally polarized spectra. Vertical expansions of the thermally polarized spectra are shown in the dashed frame (peaks a–f). (b) Representative reactions

in the mechanism for pairwise hydrogenation and isomerization of cyclopropane. Reproduced with permission from ref <sup>47</sup>, copyright 2020 American Chemical Society.

## 4.3 Surface mediated singlet-to-hyperpolarization conversion over Pt<sub>3</sub>Sn iNPs

Zhao et al. recently reported a new type of parahydrogen enhanced polarization phenomenon occurring on the surface of Pt<sub>3</sub>Sn@mSiO<sub>2</sub> iNPs: surface-mediated hyperpolarization of liquid water, methanol, and ethanol from parahydrogen.<sup>48</sup> Upon co-adsorption of parahydrogen with a deuterated solvent molecule (e.g., water, methanol, or ethanol), a non-equilibrium hyperpolarization of the isotopic impurity solvent protons spontaneously develops. The demonstration was carried out in a suspension of insoluble Pt<sub>3</sub>Sn@mSiO<sub>2</sub> iNPs in 99.9% deuterated liquid solvent under a few bars of pressure. After pH<sub>2</sub> was bubbled through the suspension for 20s at ~100 °C in the Earth's magnetic field, the tube was quickly transferred to the NMR probe for collection of the 400 MHz spectrum, shown in Figure 8. The proton signals of the exchangeable -OH protons are seen in the emission phase, characteristic of a non-equilibrium population inversion. Furthermore, the proton signals of the non-exchangeable methyl and methylene groups can also be seen in d-methanol and d-ethanol, respectively. The lower spectra were acquired when the experiments were repeated with normal H<sub>2</sub> and showed only incompletely thermally polarized absorption phase signals.

Work is underway to fully understand the mechanism underpinning surface-mediated hyperpolarization from parahydrogen. The key to this novel phenomenon appears to be the surface structure of the Pt<sub>3</sub>Sn@mSiO<sub>2</sub> catalyst. As noted above, the presence of three-fold Pt hollow sites allows the catalyst to readily dissociate and adsorb H<sub>2</sub>, while Sn serves to restrict H adatom

diffusion, while bearing an electropositive atom that can interact with oxygen in the water or alcohol to immobilize it during polarization transfer.

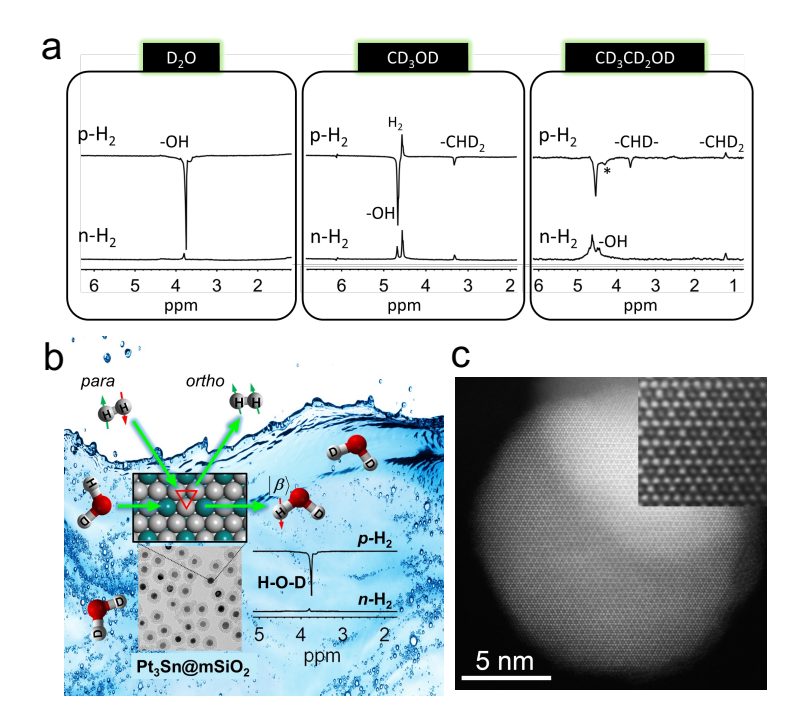


Figure 8. a) 400 MHz proton NMR spectra of hyperpolarized water, methanol, and ethanol, produced by surface-mediated singlet conversion catalysis over Pt<sub>3</sub>Sn@mSiO<sub>2</sub> iNPs. Spectra were acquired immediately after bubbling of pH<sub>2</sub> (upper spectra) or nH<sub>2</sub> (lower spectra) through a suspension in water-d<sub>2</sub> (D<sub>2</sub>O), methanol-d<sub>4</sub> (CD<sub>3</sub>OD), and ethanol-d<sub>6</sub> (CD<sub>3</sub>CD<sub>2</sub>OD). b) Artist's rendition of the effect. Reproduced with permission from ref <sup>48</sup>, copyright 2018 Cell Press.

Hyperpolarized liquid water, which is already producible to very high polarization levels by dissolution dynamic nuclear polarization (dDNP), is regarded as an "authentic" contrast agent to study localized angiography and brain perfusion,<sup>49</sup> and can be used to detect protein-ligand interactions and drug discovery. Pure hyperpolarized water, free of free radicals, catalyst residues,

or other additives, would offer greater simplicity, scalability, and portability when produced from parahydrogen. This could enable low-field magnetic resonance imaging (MRI) without superconducting magnets, providing wider access to this powerful medical diagnostic technique.

#### **Conclusion and Outlook**

In this Account, we have reviewed and highlighted the recent efforts in developing intermetallic nanocatalysts from our laboratory. Primarily, we focused on designing core-shell structured intermetallic catalysts with silica encapsulation and applying them to various thermo- and electrocatalysis reactions. They have shown excellent catalytic performances and improved our understanding of catalyst behavior at the atomic scale. In addition, we have achieved significant enhancement in the field of pairwise hydrogenation with our intermetallic catalysts.

Despite these accomplishments from our laboratory and other researchers in the field, there are still challenges yet to be addressed. First, a simple and versatile method to synthesize ultrasmall iNPs is still highly desired, especially one that adapts to different compositions and crystal structures of intermetallic compounds. Secondly, further improvement on catalytic conversion and selectivity is critical. For example, in many current cases, the improvement of catalytic selectivities is accompanied by decreased conversions. A profound understanding of the improved catalytic properties will contribute to the development of intermetallic catalysts with further enhanced performance and potential industrial applications. At the same time, such understanding of the catalysts usually requires advanced characterization techniques, and it is essential to design experiments for a better correlation between structural properties and catalytic performance. For example, performing HR-TEM or XAS experiments in situ or under operando conditions would significantly improve the understanding of catalytic behaviors. Lastly, the deviance between bulk

and nano-sized material is well known but insufficiently explored with intermetallic compounds.

For example, many intermetallic phases described in the bulk phase diagrams have not been

synthesized with any known methods at the nanoscale. Theoretical methods could provide insights

into their different formation behavior and a solution to the synthetic end. Developing new

synthetical methodologies for these nanomaterials can offer great new potentials to the catalysis

and material research fields.

**AUTHOR INFORMATION** 

**Corresponding Author** 

Wenyu Huang – Department of Chemistry, Iowa State University, Ames, Iowa 50011, United

States. Email: whuang@iastate.edu

Russ Bowers - Department of Chemistry, University of Florida, Gainesville, Florida 32611,

United States. Email: bowers@chem.ufl.edu

**Biographies** 

Minda Chen

Minda Chen received his B.A. degree in chemistry from Knox College in 2015 and is currently

pursuing a Ph.D in chemistry at Iowa State University under the supervision of Dr. Wenyu Huang.

His research interests focus on development of intermetallic nanocatalysts.

**Russ Bowers** 

31

Professor Clifford R Bowers received his B.A. majoring in Chemistry at Bowdoin College, Brunswick, Maine in 1985, and in 1990 received the Ph.D. in Chemical Physics in the group of Professor Daniel P. Weitekamp. As a NATO-NSF Postdoctoral fellow, Dr. Bowers spent a year in the lab of Prof. Michael Mehring in the 2nd Institute of Physics, University of Stuttgart, followed by a two-year postdoc with Prof. Alex Pines at the University of California, Berkeley and Lawrence Berkeley Laboratory. He joined the faculty at the University of Florida in January 1994. Bowers has contributed to developing various NMR hyperpolarization techniques, with a recent focus on parahydrogen enhanced NMR by heterogeneous catalysis.

## Wenyu Huang

Professor Wenyu Huang received his B.S. in Chemistry from Nanjing University, China, in 2000. After receiving his MS in 2002 also from Nanjing University, he started his Ph.D. research with Professor Mostafa A. El-Sayed at Georgia Institute of Technology and received his PhD in 2007. Dr. Huang then began postdoctoral research with Professor Gabor A. Somorjai and Professor Peidong Yang at University of California, Berkeley and Lawrence Berkeley National Laboratory in 2007. He joined the faculty at Iowa State University in 2011. His current research interest involves nanomaterials, heterogeneous catalysis, and polymer upcycling.

#### ACKNOWLEDGMENT

This work was supported by NSF grants CHE-2108306 and CHE-2108307. We sincerely thank Raghu V. Maligal-Ganesh, Zhiyuan Qi, Evan Wenbo Zhao, Yong Du, and Yuchen Pei for their valuable contribution during the writing of this Account.

### **ABBREVIATIONS**

iNPs, intermetallic nanoparticles; STEM, scanning transmission electron microscopy; XAS, X-ray absorption spectroscopy; mSiO<sub>2</sub>, mesoporous silica; TEM, transmission electron microscopy; EDS, energy dispersive spectroscopy; MWNT, multi-wall nanotube; PXRD, powder X-ray diffraction; CO-DRIFTS, carbon monoxide diffuse reflectance Fourier transform infrared spectroscopy; TOF, turnover frequency; MOR, methanol oxidation reaction; NMR, nuclear magnetic resonance; ALTADENA, adiabatic longitudinal transport after dissociation engenders net alignment; dDNP, dissolution dynamic nuclear polarization; MRI, magnetic resonance imaging.

#### REFERENCES

- (1) Xiao, W.; Lei, W.; Gong, M.; Xin, H. L.; Wang, D. Recent Advances of Structurally Ordered Intermetallic Nanoparticles for Electrocatalysis. *ACS Catal.* **2018**, 8, 3237-3256.
- (2) Ma, S.; Sadakiyo, M.; Heima, M.; Luo, R.; Haasch, R. T.; Gold, J. I.; Yamauchi, M.; Kenis, P. J. A. Electroreduction of Carbon Dioxide to Hydrocarbons Using Bimetallic Cu-Pd Catalysts with Different Mixing Patterns. *J. Am. Chem. Soc.* **2017**, *139*, 47-50.
- (3) Furukawa, S.; Komatsu, T. Intermetallic Compounds: Promising Inorganic Materials for Well-Structured and Electronically Modified Reaction Environments for Efficient Catalysis. *ACS Catal.* **2017**, *7*, 735-765.
- (4) Dasgupta, A.; Rioux, R. M. Intermetallics in catalysis: An exciting subset of multimetallic catalysts. *Catal. Today* **2019**, *330*, 2-15.
- (5) Zhou, M.; Li, C.; Fang, J. Noble-Metal Based Random Alloy and Intermetallic Nanocrystals: Syntheses and Applications. *Chem. Rev.* **2021**, *121*, 736-795.
- (6) Williams, B. P.; Qi, Z.; Huang, W.; Tsung, C. K. The impact of synthetic method on the catalytic application of intermetallic nanoparticles. *Nanoscale* **2020**, *12*, 18545-18562.
- (7) Li, J.; Sun, S. Intermetallic Nanoparticles: Synthetic Control and Their Enhanced Electrocatalysis. *Acc. Chem. Res.* **2019**, *52*, 2015-2025.
- (8) Yin, Z.; Lin, L.; Ma, D. Construction of Pd-based nanocatalysts for fuel cells: opportunities and challenges. *Catal. Sci. Technol.* **2014**, *4*, 4116-4128.
- (9) Han, A.; Zhang, J.; Sun, W.; Chen, W.; Zhang, S.; Hang, Y.; Feng, Q.; Zheng, L.; Gu, L.; Chen, C.; Peng, Q.; Wang, D.; Li, Y. Isolating contiguous Pt atoms and forming Pt-Zn

intermetallic nanoparticles to regulate selectivity in 4-nitrophenylacetylene hydrogenation. *Nat. Commun.* **2019**, *10*, 3787.

- (10) Chen, B. W. J.; Xu, L.; Mavrikakis, M. Computational Methods in Heterogeneous Catalysis. *Chem. Rev.* **2021**, *121*, 1007-1048.
- (11) De Vrieze, J. E.; Bremmer, G. M.; Aly, M.; Navarro, V.; Thybaut, J. W.; Kooyman, P. J.; Saeys, M. Shape of Cobalt and Platinum Nanoparticles Under a CO Atmosphere: A Combined In Situ TEM and Computational Catalysis Study. *ACS Catal.* **2019**, *9*, 7449-7456.
- (12) Maligal-Ganesh, R. V.; Xiao, C. X.; Goh, T. W.; Wang, L. L.; Gustafson, J.; Pei, Y. C.; Qi, Z. Y.; Johnson, D. D.; Zhang, S. R.; Tao, F.; Huang, W. Y. A Ship-in-a-Bottle Strategy To Synthesize Encapsulated Intermetallic Nanoparticle Catalysts: Exemplified for Furfural Hydrogenation. *ACS Catal.* **2016**, *6*, 1754-1763.
- (13) Pei, Y.; Maligal-Ganesh, R. V.; Xiao, C.; Goh, T.-W.; Brashler, K.; Gustafson, J. A.; Huang, W. An inorganic capping strategy for the seeded growth of versatile bimetallic nanostructures. *Nanoscale* **2015**, *7*, 16721-16728.
- (14) Ghosh Chaudhuri, R.; Paria, S. Core/Shell Nanoparticles: Classes, Properties, Synthesis Mechanisms, Characterization, and Applications. *Chem. Rev.* **2012**, *112*, 2373-2433.
- (15) Pei, Y.; Chen, M.; Zhong, X.; Zhao, T. Y.; Ferrer, M.-J.; Maligal-Ganesh, R. V.; Ma, T.; Zhang, B.; Qi, Z.; Zhou, L.; Bowers, C. R.; Liu, C.; Huang, W. Pairwise semi-hydrogenation of alkyne to cis-alkene on platinum-tin intermetallic compounds. *Nanoscale* **2020**, *12*, 8519-8524.

- (16) Pei, Y.; Qi, Z.; Goh, T. W.; Wang, L.-L.; Maligal-Ganesh, R. V.; MacMurdo, H. L.; Zhang, S.; Xiao, C.; Li, X.; Tao, F.; Johnson, D. D.; Huang, W. Intermetallic structures with atomic precision for selective hydrogenation of nitroarenes. *J. Catal.* **2017**, *356*, 307-314.
- (17) Chen, M.; Han, Y.; Goh, T. W.; Sun, R.; Maligal-Ganesh, R. V.; Pei, Y.; Tsung, C. K.; Evans, J. W.; Huang, W. Kinetics, energetics, and size dependence of the transformation from Pt to ordered PtSn intermetallic nanoparticles. *Nanoscale* **2019**, *11*, 5336-5345.
- (18) Qi, Z. Y.; Xiao, C. X.; Liu, C.; Goh, T. W.; Zhou, L.; Maligal-Ganesh, R.; Pei, Y. C.; Li, X. L.; Curtiss, L. A.; Huang, W. Y. Sub-4 nm PtZn Intermetallic Nanoparticles for Enhanced Mass and Specific Activities in Catalytic Electrooxidation Reaction. *J. Am. Chem. Soc.* **2017**, *139*, 4762-4768.
- (19) Maligal-Ganesh, R. V.; Pei, Y.; Xiao, C.; Chen, M.; Goh, T. W.; Sun, W.; Wu, J.; Huang, W. Sub-5 nm Intermetallic Nanoparticles Confined in Mesoporous Silica Wells for Selective Hydrogenation of Acetylene to Ethylene. *ChemCatChem* **2020**, *12*, 3022-3029.
- (20) Ma, T.; Wang, S.; Chen, M.; Maligal-Ganesh, R. V.; Wang, L.-L.; Johnson, D. D.; Kramer, M. J.; Huang, W.; Zhou, L. Toward Phase and Catalysis Control: Tracking the Formation of Intermetallic Nanoparticles at Atomic Scale. *Chem* **2019**, *5*, 1235-1247.
- (21) Chen, M.; Yan, Y.; Gebre, M.; Ordonez, C.; Liu, F.; Qi, L.; Lamkins, A.; Jing, D.; Dolge, K.; Zhang, B.; Heintz, P.; Shoemaker, D. P.; Wang, B.; Huang, W. Thermal Unequilibrium of PdSn Intermetallic Nanocatalysts: From In Situ Tailored Synthesis to Unexpected Hydrogenation Selectivity. *Angew Chem Int Ed* **2021**, *60*, 18309-18317.
- (22) Yan, Y.; Du Jingshan, S.; Gilroy Kyle, D.; Yang, D.; Xia, Y.; Zhang, H. Intermetallic Nanocrystals: Syntheses and Catalytic Applications. *Adv. Mater.* **2017**, 29, 1605997.

- (23) Nørskov, J. K.; Bligaard, T.; Rossmeisl, J.; Christensen, C. H. Towards the computational design of solid catalysts. *Nat. Chem.* **2009**, *1*, 37-46.
- (24) Gong, Y.; Wu, J.; Kitano, M.; Wang, J.; Ye, T.-N.; Li, J.; Kobayashi, Y.; Kishida, K.; Abe, H.; Niwa, Y.; Yang, H.; Tada, T.; Hosono, H. Ternary intermetallic LaCoSi as a catalyst for N2 activation. *Nat. Catal.* **2018**, *1*, 178-185.
- (25) Wegener, E. C.; Bukowski, B. C.; Yang, D.; Wu, Z.; Kropf, A. J.; Delgass, W. N.; Greeley, J.; Zhang, G.; Miller, J. T. Intermetallic Compounds as an Alternative to Single-atom Alloy Catalysts: Geometric and Electronic Structures from Advanced X-ray Spectroscopies and Computational Studies. *ChemCatChem* **2020**, *12*, 1325-1333.
- (26) Zhao, E. W.; Maligal Ganesh, R.; Xiao, C.; Goh, T. W.; Qi, Z.; Pei, Y.; Hagelin Weaver Helena, E.; Huang, W.; Bowers Clifford, R. Silica Encapsulated Pt Sn Intermetallic Nanoparticles: A Robust Catalytic Platform for Parahydrogen Induced Polarization of Gases and Liquids. *Angew. Chem. In. Ed.* **2017**, *56*, 3925-3929.
- (27) Li, D.; Wang, C.; Tripkovic, D.; Sun, S.; Markovic, N. M.; Stamenkovic, V. R. Surfactant Removal for Colloidal Nanoparticles from Solution Synthesis: The Effect on Catalytic Performance. *ACS Catal.* **2012**, *2*, 1358-1362.
- (28) Lopez-Sanchez, J. A.; Dimitratos, N.; Hammond, C.; Brett, G. L.; Kesavan, L.; White, S.; Miedziak, P.; Tiruvalam, R.; Jenkins, R. L.; Carley, A. F.; Knight, D.; Kiely, C. J.; Hutchings, G. J. Facile removal of stabilizer-ligands from supported gold nanoparticles. *Nat. Chem.* **2011**, *3*, 551-556.
- (29) Naresh, N.; Wasim, F. G. S.; Ladewig, B. P.; Neergat, M. Removal of surfactant and capping agent from Pd nanocubes (Pd-NCs) using tert-butylamine: its effect on electrochemical characteristics. *J. Mater. Chem. A* **2013**, *1*, 8553-8559.

- (30) Wu, B.; Huang, H.; Yang, J.; Zheng, N.; Fu, G. Selective Hydrogenation of α,β-Unsaturated Aldehydes Catalyzed by Amine-Capped Platinum-Cobalt Nanocrystals. *Angew*. *Chem. Int. Ed.* **2012**, *51*, 3440-3443.
- (31) Vu, K. B.; Bukhryakov, K. V.; Anjum, D. H.; Rodionov, V. O. Surface-Bound Ligands Modulate Chemoselectivity and Activity of a Bimetallic Nanoparticle Catalyst. *ACS Catal.* **2015**, *5*, 2529-2533.
- (32) Niu, Y.; Liu, X.; Wang, Y.; Zhou, S.; Lv, Z.; Zhang, L.; Shi, W.; Li, Y.; Zhang, W.; Su, D. S.; Zhang, B. Visualizing Formation of Intermetallic PdZn in a Palladium/Zinc Oxide Catalyst: Interfacial Fertilization by PdHx. *Angew. Chem. Int. Ed.* **2019**, *58*, 4232-4237.
- (33) Furukawa, S.; Yoshida, Y.; Komatsu, T. Chemoselective Hydrogenation of Nitrostyrene to Aminostyrene over Pd- and Rh-Based Intermetallic Compounds. *ACS Catal*. **2014**, *4*, 1441-1450.
- (34) Yang, N.; Zhang, Z.; Chen, B.; Huang, Y.; Chen, J.; Lai, Z.; Chen, Y.; Sindoro, M.; Wang, A.-L.; Cheng, H.; Fan, Z.; Liu, X.; Li, B.; Zong, Y.; Gu, L.; Zhang, H. Synthesis of Ultrathin PdCu Alloy Nanosheets Used as a Highly Efficient Electrocatalyst for Formic Acid Oxidation. *Adv. Mater.* **2017**, *29*, 1700769.
- (35) Pei, Y.; Zhang, B.; Maligal-Ganesh, R. V.; Naik, P. J.; Goh, T. W.; MacMurdo, H. L.; Qi, Z.; Chen, M.; Behera, R. K.; Slowing, I. I.; Huang, W. Catalytic properties of intermetallic platinum-tin nanoparticles with non-stoichiometric compositions. *J. Catal.* **2019**, *374*, 136-142.
- (36) Bowers, C. R.; Weitekamp, D. P. Parahydrogen and synthesis allow dramatically enhanced nuclear alignment. *J. Am. Chem. Soc.* **1987**, *109*, 5541-5542.

- (37) Bowers, C. R.: Sensitivity Enhancement Utilizing Parahydrogen. In *eMagRes*; Harris, R. K., Wasylishen, R. L., Eds., 2007.
- (38) Kovtunov, K. V.; Beck, I. E.; Bukhtiyarov, V. I.; Koptyug, I. V. Observation of Parahydrogen-Induced Polarization in Heterogeneous Hydrogenation on Supported Metal Catalysts. *Angew. Chem. Int. Ed.* **2008**, *47*, 1492-1495.
- Zhao, E. W.; Zheng, H.; Ludden, K.; Xin, Y.; Hagelin-Weaver, H. E.; Bowers, C.
  R. Strong Metal–Support Interactions Enhance the Pairwise Selectivity of Parahydrogen
  Addition over Ir/TiO2. ACS Catal. 2016, 6, 974-978.
- (40) Song, B.; Choi, D.; Xin, Y.; Bowers, C. R.; Hagelin-Weaver, H. Ultra-Low Loading Pt/CeO2 Catalysts: Ceria Facet Effect Affords Improved Pairwise Selectivity for Parahydrogen Enhanced NMR Spectroscopy. *Angew. Chem. Int. Ed.* **2021**, *60*, 4038-4042.
- (41) Zhivonitko, V. V.; Kovtunov, K. V.; Beck, I. E.; Ayupov, A. B.; Bukhtiyarov, V. I.; Koptyug, I. V. Role of Different Active Sites in Heterogeneous Alkene Hydrogenation on Platinum Catalysts Revealed by Means of Parahydrogen-Induced Polarization. *J. Phys. Chem. C* **2011**, *115*, 13386-13391.
- (42) Fearon, J.; Watson, G. W. Hydrogen adsorption and diffusion on Pt {111} and PtSn {111}. *J. Mater. Chem.* **2006**, *16*, 1989-1996.
- (43) Pravica, M. G.; Weitekamp, D. P. Net NMR alignment by adiabatic transport of parahydrogen addition products to high magnetic field. *Chem. Phys. Lett.* **1988**, *145*, 255-258.
- (44) Paffett, M. T.; Gebhard, S. C.; Windham, R. G.; Koel, B. E. Chemisorption of carbon monoxide, hydrogen, and oxygen on ordered tin/platinum(111) surface alloys. *J. Phys. Chem.* **1990**, *94*, 6831-6839.

- (45) Salnikov, O. G.; Kovtunov, K. V.; Nikolaou, P.; Kovtunova, L. M.; Bukhtiyarov, V. I.; Koptyug, I. V.; Chekmenev, E. Y. Heterogeneous Parahydrogen Pairwise Addition to Cyclopropane. *ChemPhysChem* **2018**, *19*, 2621-2626.
- (46) Pedersen, S.; Herek, J. L.; Zewail, A. H. The Validity of the "Diradical" Hypothesis: Direct Femtoscond Studies of the Transition-State Structures. *Science* **1994**, 266, 1359.
- (47) Du, Y.; Behera, R.; Maligal-Ganesh, R. V.; Chen, M.; Chekmenev, E. Y.; Huang, W.; Bowers, C. R. Cyclopropane Hydrogenation vs Isomerization over Pt and Pt–Sn Intermetallic Nanoparticle Catalysts: A Parahydrogen Spin-Labeling Study. *J. Phys. Chem. C* **2020**, *124*, 8304-8309.
- (48) Zhao, E. W.; Maligal-Ganesh, R.; Du, Y.; Zhao, T. Y.; Collins, J.; Ma, T.; Zhou, L.; Goh, T.-W.; Huang, W.; Bowers, C. R. Surface-Mediated Hyperpolarization of Liquid Water from Parahydrogen. *Chem* **2018**, *4*, 1387-1403.
- (49) Ardenkjær-Larsen, J. H.; Fridlund, B.; Gram, A.; Hansson, G.; Hansson, L.; Lerche, M. H.; Servin, R.; Thaning, M.; Golman, K. Increase in signal-to-noise ratio of > 10,000 times in liquid-state NMR. *Proc. Natl. Acad. Sci. U.S.A.* **2003**, *100*, 10158.

# **Table of Content**

